Published in final edited form as:

Phys Med Biol. 2016 July 7; 61(13): 4763–4780. doi:10.1088/0031-9155/61/13/4763.

Evaluation of the Effect of Transcytolemmal Water Exchange Analysis for Therapeutic Response Assessment using DCE-MRI: A Comparison Study

Chunhao Wang, **Ergys Subashi**, **Xiao Liang**, **Fang-Fang Yin**, and **Zheng Chang***

Department of Radiation Oncology, Duke University Medical Center, Durham, North Carolina, 27710, United States

Abstract

This study compares the Shutter-Speed (SS) and the Tofts models as used in assessing therapeutic response in a longitudinal DCE-MRI experiment. Sixteen *nu/nu* mice with implanted colorectal adenocarcinoma cell line (LS-174T) were randomly assigned into treatment/control groups (n=8/group) and received bevacizumab/saline twice weekly (Day1/Day4/Day8). All mice were scanned at one pre- (Day0) and two post-treatment (Day2/Day9) time points using a high spatiotemporal resolution DCE-MRI pulse sequence. The CA extravasation rate constant K_T^{trans}/K_S^{trans} from the Tofts/SS model and the mean intracellular water residence time τ_i from the SS model were analyzed. A biological subvolume (BV) within the tumor was identified based on the τ_i intensity distribution, and the SS model parameters within the BV ($K_{S,BV}^{trans}$ and $\tau_{i,BV}$) were analyzed. It is found that K_S^{trans} and K_T^{trans} have a similar spatial distribution in the tumor volume. The Bayesian information criterion (BIC) results show that the SS model was a better fit for all scans. At Day9, the treatment group had significantly higher tumor mean K_T^{trans} (p=0.021), K_S^{trans} (p=0.021) and τ_i (p=0.045). When BV from transcytolemmal water exchange analysis was adopted, the treatment group had higher mean $K_{S,BV}^{trans}$ at both Day2 (p=0.038) and Day9 (p=0.007). Additionally, at Day9, the treatment group had higher mean $\tau_{i,BV}$ (p=0.045) and higher $K_{S,BV}^{trans}$ spatial heterogeneity indices (Rényi dimensions) d_1 (p=0.010) and d_2 (p=0.021). When mean $K_{S,BV}^{trans}$ and its coefficient of variation (CV) were used to separate treatment/control group samples using supporting vector machine (SVM), the accuracy of treatment/control classification was 68.8% at Day2 and 87.5% at Day9; in contrast, the Day2/Day9 accuracy were 62.5%/87.5% using tumor mean K_S^{trans} and its CV and were 50.0%/87.5% using tumor mean K_T^{trans} and its CV, respectively. These results suggest that the SS model parameters outperformed the Tofts model parameters in terms of capturing bevacizumab therapeutic effect in this longitudinal experiment.

*Corresponding author: Zheng Chang, Ph.D., Department of Radiation Oncology, Duke University Medical Center, Durham, NC 27710, Telephone: (919) 681-2608, Fax: (919) 681-7183, zheng.chang@duke.edu.

Keywords

DCE-MRI; transcytolemmal water exchange; small animal experiment; therapeutic response assessment

1. Introduction

Dynamic contrast-enhanced magnetic resonance imaging (DCE-MRI) is an imaging technique used for functional non-invasive measurements of microvascular properties. Based on the fast acquisition of a series of images before, during, and after the intravenous administration of a low molecular weight contrast agent (CA), DCE-MRI can measure differences in microvessel physiology associated with tumor angiogenesis (Hylton, 2006). Quantitative pharmacokinetic (PK) and heuristic model-based parameters have been established to characterize *in-vivo* microvascular features including blood volume, blood flow and vascular permeability (O'Connor *et al.*, 2007). Compared to CT in characterizing microvascular function, DCE-MRI involves no use of ionizing radiation (Kershaw and Buckley, 2006) and has the additional merit of combining morphological and functional information in a single imaging session without sacrificing spatial resolution (Choyke *et al.*, 2003). Because of these advantages, DCE-MRI is considered as a promising imaging technique for tumor staging (Delongchamps *et al.*, 2011) and treatment planning (van der Heide *et al.*, 2012). In the area of treatment response assessment, DCE-MRI is also capable of monitoring the therapeutic effect of radiotherapy (Cabrera *et al.*, 2013; Wang *et al.*, 2015), chemotherapy (Abramson *et al.*, 2013; Yankeelov *et al.*, 2007) and anti-vascular drugs (O'Connor *et al.*, 2012).

Therapeutic response is commonly quantified by morphological descriptors of tumor volume (Jaffe, 2006) and first order statistics (mean/median/variance) of the PK parameters over the entire tumor volume or within manually selected regions of interest (ROIs) (O'Connor *et al.*, 2011). However, human solid tumors are reported to be heterogeneous in terms of CA kinetic characteristics (Parker *et al.*, 1997), and the current statistics for treatment response assessment cannot fully quantify tumor heterogeneity. For the purpose of automated extraction of image features with great throughput potentials for computer-aided diagnosis and outcome prediction (which recently can be referred as Radiomics) (Aerts *et al.*, 2014), the tumor heterogeneity extracted from the texture analysis of PK parametric maps have been incorporated as a key component for DCE-MRI characterization (Lambin *et al.*, 2012; Jiang *et al.*, 1999). Pilot studies have demonstrated the use of tumor heterogeneity as a biomarker for treatment assessment (Alic *et al.*, 2011; Goh *et al.*, 2011; Rose *et al.*, 2009; Yang and Knopp, 2011). To ensure the prompt capture of treatment induced functional changes, the derivation of PK parameters needs to be accurate and precise (Chang and Wang, 2015). So far, the most widely used PK model is the one proposed by Tofts and Kermode (Tofts and Kermode, 1991) in which the CA kinetics in the microvessel environment is described by the CA bidirectional transendothelium exchange between two compartments, blood plasma and extravascular-extracellular space (EES). Prior to model fitting, the CA concentration maps at each post-injection time point need to be determined. The conversion of MR signal to CA concentration is frequently reported as a linear

relationship between the CA concentration and the change of longitudinal relaxation rate $R_1 = (1/T_1)$. Such linear relationship relies on the assumption that the extravascular space is a single well-mixed medium and thus the interstitium can be treated as a homogeneous solution. Hence, it is required that water exchange from the intracellular space to EES (also known as transcytolemmal water exchange) must be sufficiently fast. However, biological tissue could be highly compartmentalized on a histological scale (Landis *et al.*, 1999) and the assumption of fast transcytolemmal water exchange (Fast-Exchange Limit FXL) may not always be satisfied. If the transcytolemmal water exchange is not fast enough to equilibrate the effects of CA in EES, the aforementioned linear relationship between the CA concentration and the change of longitudinal relaxation would be violated (Labadie *et al.*, 1994). In practice, the Bloch equations should incorporate the effects of the limited transcytolemmal water exchange rate with a bi-exponential decay term of longitudinal relaxation (Landis *et al.*, 2000). The main result of this modification is known as the shutter-speed (SS) model (Yankeelov *et al.*, 2003). In this model, the transcytolemmal water exchange rate is modelled as the inverse of the mean residence time of water molecules in the intracellular space, and the relationship between the CA concentration and longitudinal relaxation rate change is expressed as a nonlinear equation with the presence of limited transcytolemmal water exchange rate.

The SS model has been applied for the PK characterization of head and neck cancer (Kim *et al.*, 2010; Kim *et al.*, 2007), breast cancer (Huang *et al.*, 2008) and prostate cancer (Li *et al.*, 2013). For treatment response assessment, this model has been investigated in a limited number of clinical studies (Huang *et al.*, 2014; Yankeelov *et al.*, 2007). However, to our best knowledge, a comprehensive comparison of the SS model and the classic Tofts model in capturing therapeutic response effect has not been fully explored, especially with the comparison of randomized treatment/control groups in a longitudinal experiment setup with multiple post-treatment evaluation. The present work was conducted to evaluate the performance of the SS model with transcytolemmal water exchange analysis in a small animal therapeutic response assessment experiment with high spatiotemporal resolution DCE-MRI. The potential use of first order statistics, histogram descriptors and spatial heterogeneity indices of the PK parametric maps from both models were investigated at multiple time points.

2. Materials and methods

Small Animal Experiment

All animal studies were approved by the Institutional Animal Care and Use Committee. In this longitudinal experiment, a total of 16 female *nu/nu* mice with a colorectal adenocarcinoma cell line LS-174T (Charles River Laboratories, Wilmington, MA) implanted in the mammary fat pad were followed for four weeks. The mice were randomly assigned into the equally-sized treatment group or the control group (n = 8/group) when tumor volume was approximately 100μL. A pre-treatment DCE-MRI scan was acquired at Day0 as the baseline. The treatment/control group received bevacizumab (Avastin®, Genentech, South San Francisco, CA) or normal saline via an intraperitoneal injection at a dose of 5 mg/kg or 5 mL/kg twice weekly. Two post-treatment DCE-MRI scans were

performed weekly. The first two post-treatment scans at Day2 and Day9 were evaluated since the therapeutic effects of the treatment group were prominent after the first two weeks' experiment.

DCE-MRI Protocol

All DCE-MRI scans were performed in a 7T small animal MRI scanner (Bruker BioSpin MRI GmbH, Ettlingen, Germany) equipped with self-shielded gradient coils with a maximum strength of 450 *mT/m* and a rise time of 110 μs. An actively detuned volume RF coil (linear transmit, ID = 72 mm) was used in conjunction with a four-element coil (2×2 linear array, 10×10 mm loops) for surface receive. An interleaved ultra-short-echo radial sampling sequence was adopted for 4D reconstruction using a sliding-window keyhole approach as described in previous work (Subashi *et al.*, 2013). The acquisition parameters were listed as follows: FOV = 20×20×20 mm^3, matrix = 128×128×128, TR/TE = 5/0.02 ms, NEX = 1, flip angle $\alpha = 10°$, temporal resolution = 9.9s, spatial resolution = 156μm. Using this pulse sequence, the selection of TE=0.02 ms allows for the application of the SPGR equation without T2* corrections (Kleppestø *et al.*, 2014), and the calculated CA concentrations have been shown to be within the theoretically predicted uncertainty (Subashi *et al.*, 2014). Prior to the CA injection, two calibration scans with $\alpha = \{2°, 10°\}$ were acquired to calculate the native longitudinal relaxation rate with dual flip angle calculate method (Fram *et al.*, 1987). An automatic syringe pump (KD Scientific Inc., Holliston, MA) was used to administer Gd-DTPA (Magnevist, Schering AG, Berlin, Germany) via a 27-gauge tail vein catheter at a dose of 0.5 mmol/kg and a flow rate of 2.4mL/min. The dynamic acquisition was initiated two minutes prior to the CA injection and lasted for approximately 20 minutes after the CA injection. For a well-controlled setup for dynamic imaging, animals were positioned in a custom-made MR-cradle and were maintained under anesthesia by isoflurane delivery via a nose cone. The body temperature was controlled between 36°C and 37°C by circulating warm water. Breathing was monitored through a pneumatic pillow and was maintained at a rate of 50–60 breaths/min via adjusting isoflurane delivery.

Image Analysis

For each DCE-MRI scan, the tumor volume V was measured on one of the contrast-enhanced volumes. The tumor growth rate at each post-treatment scan day was defined as the volume ratio to the pre-treatment baseline value and was selected as the primary tumor morphological descriptor. In the PK analysis using the Tofts model, the CA concentration $C(t)$ at each post-injection time point was estimated using the following linear equation:

$$C(t)=(R_1(t)-R_{10})/r_1 \quad (1)$$

where r_1 is the longitudinal relaxivity (= 3.275 $mM^{-1}s^{-1}$ at 7T) of the CA (Noebauer-Huhmann *et al.*, 2010), R_{10} is the native longitudinal relaxation rate prior to CA injection and $R_1(t)$ is the post-injection longitudinal relaxation rate (= $1/T_1$) determined by using a published method (Schabel and Parker, 2008). The two-compartment Tofts model is expressed as below with Kety rate law employed (Kety, 1960):

$$C(t)=K^{trans}\int_0^t C_p(u)\cdot e^{-(K^{trans}/v_e)\cdot(t-u)}du \quad (2)$$

where K^{trans} is the rate constant of CA extravasation from blood plasma to EES, and v_e is the volume fraction of EES. The parameter $k_{ep} = K^{trans} / v_e$ is the rate constant describing the CA transport from EES back to blood plasma. The arterial input function (AIF) $C_p(t)$ in this study was approximated by a reported population measurement (Loveless *et al.*, 2012). Eq. (2) was then solved on a voxel-by-voxel basis using a linear least-squares method (Murase, 2004).

The SS model with transcytolemmal water exchange is expressed as:

$$R_1(t)=\frac{1}{2}\left[R_{1i}+R_{1e}+r_1<CA,t>+\frac{1}{\tau_i}+\frac{1-v_e/f_w}{\tau_i v_e/f_w}\right]-\frac{1}{2}\left\{\left[R_{1i}-R_{1e}-r_1<CA,t>+\frac{1}{\tau_i}+\frac{1-v_e/f_w}{\tau_i v_e/f_w}\right]^2+\frac{4(1-v_e/f_w)}{\tau_i^2 v_e/f_w}\right\}^{1/2}$$

(3)

where R_{1i} and R_{1e} represent the native longitudinal relaxation rate of intracellular space and EES water molecules, respectively. τ_i denotes the mean residence time of water molecules in the intracellular space whose inverse represents the transcytolemmal water exchange rate constant. f_w is the fraction of water molecules in EES that are accessible to mobile CA particles, and a constant of 0.8 was chosen as previously reported (Landis *et al.*, 2000; Yankeelov *et al.*, 2007). In Eq. (3), the notation $<CA>$ represents the indirect CA concentration result at a post-injection time point, which is still related to the CA extravasation constant K^{trans} with Kety rate law:

$$<CA,t>=K^{trans}\int_0^t C_p(u)\cdot e^{-(K^{trans}/v_e)\cdot(t-u)}du \quad (4)$$

A substitution of Eq. (4) into Eq. (3) yields the operable equation of the SS model for three PK parameters: K^{trans}, v_e (or $k_{ep} = K^{trans}/ v_e$) and τ_i. R_{1i} and R_{1e} can be approximated as R_{10} in Eq. (1) (Landis *et al.*, 2000). The SS model was solved by the nonlinear least-squares fitting Levenberg-Marquardt method on a voxel-by-voxel base (Ahearn *et al.*, 2005). To avoid the potential fitting error due to the local minimum, the Levenberg-Marquardt iteration was repeated with 25 groups of randomly-selected initial points within the reported range: K^{trans}: 0–2 min^{-1}; τ_i: 0–2 s; and v_e: 0–1 ml/ml, and the result with the best fitting quality with the least χ^2 value was reported (Kim *et al.*, 2007):

$$\chi^2=\frac{1}{N}\sum_{i=1}^{N}\frac{(S_i-P_i)^2}{P_i} \quad (5)$$

where N is the length of measurement data series, S_i is the measured data (C(t) for Tofts model and R_1(t) for SS model), and P_i is the fitted data by the model.

The CA extravasation rate constant from the Tofts model (K_T^{trans}) and the SS model (K_S^{trans}) were reported as the primary PK parameters. The mean of K^{trans} within a ROI has been frequently reported as an important DCE-MRI biomarker and has been selected as the primary clinical DCE-MRI biomarker by the Quantitative Imaging Biomarker Alliance (QIBA) of Radiological Society of North America (RSNA) (Padhani and Leach, 2005; DCE-MRI-Technical-Committee, 2012). For the SS model, τ_i was also selected as an additional PK parameter. For each recorded parametric map, the tumor mean value was calculated. The coefficient of variation (CV) defined as the ratio of the standard deviation to the mean value was also reported as a measure of the parameter's probability distribution dispersion (Sokal and Rohlf, 1981). The histogram descriptors, kurtosis (measurement of 'peakedness' of the probability distribution) and skewness (measurement of asymmetry of probability distribution) were recorded to describe the shape of the intensity distribution. Inspired by initial promising work (Collins *et al.*, 2003), the classic fractal dimensions d_1 and d_2 defined by the generalized Rényi dimensions were analyzed for spatial heterogeneity measurement (Allen *et al.*, 1995). As the heterogeneity information measurement, Rényi dimensions d_1 and d_2 measure the Rényi entropy at different scales:

$$d_q = \lim_{\varepsilon \to 0} \frac{log \sum_i p_i^q}{(1-q) log \, 1/\varepsilon}$$
$$d_1 = \lim_{q \to 1} d_q \qquad (6)$$

where ε is the scale resolution (ranging from a single voxel dimension to the size of field of view) and p_i is the normalized intensity value of i-th voxel such that $\Sigma_i p_i = 1 \; \forall i$. Two heterogeneity indices of intensity object, d_1 information dimension and d_2 correlation, were adopted in this work. For objects with pre-defined shape, d_1 and d_2 values were reported for objects with larger intensity variations (Bartholdi *et al.*, 2003). Previous studies have reported that d_1 and d_2 of K^{trans} map might reflect the tumor heterogeneity differences between low and high-grade glioma (Rose *et al.*, 2009). In one of our recent works, the d_1 and d_2 of K^{trans} map were found to be useful in determining the bevacizumab therapeutic effect (Wang *et al.*, 2016).

As a further utilization of transcytolemmal water exchange analysis, for each scan, a biological subvolume (BV) within the tumor was identified based on τ_i intensity distribution. Specifically, the τ_i histogram was generated, and an intensity threshold was automatically determined based on the leftmost peak position. The BV was then identified as the voxels with τ_i intensity higher than the threshold. Within the BV, the CA extravasation rate constant ($K_{S,BV}^{trans}$) and intracellular water molecule residence time ($\tau_{i,BV}$) were analyzed. The aforementioned PK parameter metrics (mean, CV, kurtosis, skewness, d_1 and d_2) of $K_{S,BV}^{trans}$ and $\tau_{i,BV}$ were recorded.

The performance of the two models with respect to data fitting quality was estimated with the Bayesian information criterion as a commonly used statistical criteria for model selection (Schwarz, 1978):

$$BIC=\log(\chi^2)+(k\log N)/N \quad (7)$$

where N is the length of measurement data series, χ^2 is the median value of the χ^2 map from one model and k is the model freedom degree (2 for Tofts model and 3 for SS model). A smaller BIC value can be interpreted as better data fitting quality.

Statistical Analysis

Each recorded metric was compared longitudinally, and at each post-treatment scan day, the Mann-Whitney U-test was used to assess the difference of the recorded metric between treatment and control groups. Significance was determined based on a p-level less than 0.05 with multi-comparison correction if applicable (Chen *et al.*, 2007). To determine the model fitting quality, the BIC values of the Tofts model and the SS model of all examined scans were compared using Wilcoxon signed-rank test with significance level $p < 0.05$. Of all 48 scans, 2 were excluded for analysis as the CA injection was unsuccessful. To validate the potential use of the recorded metrics from PK parameter analysis for treatment/control group separation, classification experiments using support vector machine (SVM) in a leave-one-out approach were performed at each post-treatment scan day with single/multiple metric(s) as input.

3. Results

Figure 1 shows the analysis of a representative animal from the treatment group at three DCE-MRI scan days (left column: Day0; middle column: Day2; right column: Day9). The spatial heterogeneity of intensity distribution within the defined tumor can be readily appreciated in the DCE volumes about 60 seconds after the CA injection (Figure 1 (a)–(c)). The K_T^{trans} maps (Figure 1 (d)–(f)) and the K_S^{trans} maps (Figure 1 (g)–(i)) at each scan day were morphologically similar with comparable shape patterns. Compared to the K_T^{trans} maps, the K_S^{trans} maps had higher intensity values across the tumor. K^{trans} hotspots were identified at the same locations on both sets of maps, and the hotspots on K_S^{trans} maps had relatively larger sizes and higher intensities. The K^{trans} histograms (Figure 1 (j)–(l)) from both models had peak positions towards the low intensity region (i.e., positive skewness), and the K_S^{trans} were likely to exhibit higher probability towards the high intensity region. This observation is consistent with the high K^{trans} values of K_S^{trans} maps. The bevacizumab treatment effect was obvious on (f) and (i) after three doses, as the K^{trans} intensities across the tumor decreased in reference to the pre-treatment maps.

Figure 2 shows the τ_i results of the same animal in Figure 1 from the transcytolemmal water exchange analysis (left column: Day0; middle column: Day2; right column: Day9). As can be observed in Figure 2 (a)–(c), at each scan day, τ_i had an intensity-elevated region with

very clear and sharp boundary. Accordingly, the identified BV regions are presented in the 2nd row as red areas. Within these BVs, the transcytolemmal water exchange rate (= $1/\tau_i$) was relatively limited with higher τ_i values. At each scan day, the τ_i histogram Figure 3 (g)–(i) had its first peak at the leftmost bin. Based on the aforementioned BV identification method, the τ_i intensity threshold for BV was about 10ms in these three scans. The increase of probability sum of all non-zero bins was consistent with the increase of mean τ_i value along the experiment (Day0: 0.159 s; Day2: 0.170 s; Day9: 0.193 s). Such increase is also supported by the observable intensity elevation from Figure 2(d) to (f).

Figure 3 reports BIC results for the comparison of data fitting quality using the two investigated models. The median BIC value (indicated by red line) of the SS model was lower than the corresponding value of the Tofts model. Wilcoxon signed-rank test showed that the SS model's BIC values were significantly lower than the Tofts model' values (p<. 0001), indicating that the SS model has generally improved data fitting qualities than the Tofts model.

Figure 4 demonstrates the therapeutic response assessment using tumor morphological descriptors. The error bar represents the group standard deviation. At Day0, the initial tumor volumes of the treatment and control group were 115 ± 41 μL and 91 ± 37 μL, respectively. As reflected by the tumor growth rate (Figure 4 (a)), during the treatment course, the tumors in the treatment group grew slower than the tumors in the control. At the end of the experiment at Day9, the tumor growth rates of the treatment group were significantly lower than the control group rate (p = 0.002). Figure 4(b) shows the evolution of the ratio of identified BV using τ_i to the tumor volume from transcytolemmal water exchange analysis. The ratio decreased in both treatment and control groups during the experiment with no statistically significant difference.

Figure 5 summarizes the therapeutic response assessments using K_T^{trans} and K_S^{trans} metrics. Regarding tumor mean K_T^{trans} and K_S^{trans} values (Figure 5 (a)), at Day0, there was no significant difference between the treatment/control groups K_T^{trans} and K_S^{trans} value. At end of follow-up, both treatment and control groups showed a decreasing trend of K^{trans}. The CV of K_T^{trans} and K_S^{trans} of both groups (Figure 5 (b)) increased in the experiment, suggesting the increased K^{trans} probability distribution dispersion. The evaluation of K^{trans} kurtosis and skewness in (c) and (d) suggest that in both models, the peak of K^{trans} probability distribution moved towards the zero-value direction with increased peak height. The decreases of the spatial heterogeneity indices d_1 and d_2 of both groups in (e) and (f) suggest the tumor heterogeneity reduction along the experiment. At Day9, the treatment group had significantly lower K_T^{trans} (p = 0.021) and K_S^{trans} (p = 0.021) values than the control group. The other statistics including CV, kurtosis, skewness, d_1 and d_2 did not show significant difference between the treatment/control groups.

Figure 6 shows the therapeutic response assessment using τ_i from transcytolemmal water exchange analysis. As shown in (a), the tumor mean τ_i of the treatment group increased during the experiment, while the control group values were relatively stable. At Day9, the treatment group had significantly higher mean τ_i values (p = 0.045). While the control group

τ_i CVs kept increasing in (b), the treatment group τ_i CV increased from Day0 to Day2 but was relatively stable from Day2 to Day9. The τ_i CV difference between treatment/control groups was not statistically significant. Unlike the decreasing trend of K_T^{trans} and K_S^{trans} spatial heterogeneity indices, the d_1 and d_2 values of τ_i were relatively stable in both treatment/control groups with no significant difference, though the d_2 differences at Day2 showed a trend towards significance ($p = 0.083$). The evaluations of kurtosis and skewness were not reported since all τ_i histograms had their first peak at the first bin and thus the histogram descriptors comparison became trivial.

Figure 7 shows the results using $K_{S,BV}^{trans}$ and $\tau_{i,BV}$ within the identified BVs with boxplot comparisons as the identified BV at different days were not necessarily overlapped. As shown in (a), the mean $K_{S,BV}^{trans}$ across the BV had higher intensities in comparison with Figure 5(a), and the decreasing trend in both treatment/control groups was observed. It is important to point out that the treatment group had significantly lower mean $K_{S,BV}^{trans}$ values at both Day2 ($p = 0.038$) and Day9 ($p = 0.007$), while the treatment group had significantly lower mean $K_{S,}^{trans}$ values only at Day9 ($p = 0.021$) in Figure 5(a). This suggests a potential value of $K_{S,BV}^{trans}$ for early capture of bevacizumab therapeutic effect. Similarly to τ_i results in Figure 6(b), the treatment group had significantly higher $\tau_{i,BV}$ values at Day9 ($p = 0.045$). Additionally, the spatial heterogeneity indices in (c) and (d) show that the treatment group had significantly higher $K_{S,BV}^{trans}$ d_1 ($p = 0.010$) and d_2 ($p = 0.021$) values after the experiment at Day9. The other comparisons of $K_{S,BV}^{trans}$ and $\tau_{i,BV}$ metrics did not show significant difference between treatment/control groups. These results in Figure 7 suggest that the identified BV could provide additional benefits for early treatment response assessment using K^{trans} and τ_i statistics.

Table 1 summarizes the results of treatment/control groups' classification experiments using SVM. When the tumor mean value of K_T^{trans} or K_S^{trans} was selected as the sole parameter for SVM, the classification accuracy at Day9 was 68.8%. In contrast, the accuracy at Day9 using mean $K_{S,BV}^{trans}$ as the input was as high as 87.5%. When CV was used along with tumor mean K_T^{trans} and tumor mean K_S^{trans}, the classification accuracy at Day9 were improved to 87.5% and 87.5%, respectively. With BV information, the Day2 classification accuracy using mean $K_{S,BV}^{trans}$ and its CV were improved from 62.5% to 68.8%, while the Day9 accuracy remained 87.5% without improvement. The classifications tests using τ_i/$\tau_{i,BV}$ metrics were suboptimal than the tests using K^{trans} metrics from both models, as the highest achievable accuracy at Day9 were 62.5% using mean $\tau_{i,BV}$ and its CV. As a general summary of Table 1, the treatment/control group classification using K^{trans} across the whole tumor from the Tofts model and the SS model were comparable at Day9; when using K^{trans} statistics the identified BV, the classification accuracies at Day2 were further improved.

4. Discussion

In this work, the therapeutic response assessment using the classic Tofts model and the SS model with transcytolemmal water exchange analysis were compared in a longitudinal small animal study. This study used bevacizumab as a recombinant humanized monoclonal IgG_1 antibody that selectively binds to and neutralizes the functional activity of vascular endothelial growth factor (VEGF) (Jain *et al.*, 2006). Such neutralization can lead to the reduction of tumor vascularization and the decrease of lesion volume, which reflects an effective response and would be the desirable treatment outcome function (Cohen *et al.*, 2007). In this study, the application of bevacizumab caused a decrease of tumor growth rate, though complete tumor regression was not achieved. This may explain the observation that some of the investigated metrics of the treatment and the control groups showed similar evolution trends during the experiment.

As the primary functional imaging biomarker from the quantitative PK analysis, the parameter K^{trans} describes the combined information of capillary wall surface, capillary permeability, and blood flow. As shown in Figure 1 and Figure 5(a), the tumor mean values of K_S^{trans} from the SS model were higher than the tumor mean values K_T^{trans} from the classic Tofts model. This result was consistent with the previously reported results about larger K_S^{trans} (Huang *et al.*, 2014; Kim *et al.*, 2007). As another potential parameter-of-interest, the tumor mean CA rate constant k_{ep} ($=K^{trans}/v_e$) results from both models were summarized as Figure S1 in the supplementary document. For a short conclusion, in both treatment and control group, k_{ep} from both models showed a decreasing trend during the experiment, and no statistically significant difference were found between treatment/control groups' values at Day2/Day9. The inclusion of limited transcytolemmal water exchange rate has been argued to consider the CA particles that cannot be immediately distributed in EES. Thus, the SS model yielded higher CA concentrations and thus higher CA extravasation rate values in comparison with the classic Tofts model. When the injected CA dose is high (0.5 mmol/kg body weight in this work), the adoption of SS model becomes necessary to correct the CA concentration underestimation (Yankeelov *et al.*, 2005). The K^{trans} maps identified by the two models were morphologically comparable in Figure 1, and the SS model was found to be a better fit for all scans in terms of BIC comparison in Figure 3. These results may serve as the evidence that SS model could describe the microvessel environment more accurately than the classic Tofts model. The histology report would be valuable as the gold standard for the correlation study with PK parametric maps. The histology report after the 2nd post-treatment imaging was not included in this experiment. For our ongoing and future experiments, the histology report will be included as an essential component for direct evaluation of PK model validity.

Many studies have reported a decreased tumor mean K^{trans} value after bevacizumab application or its combination with other treatment regimens (Cabrera *et al.*, 2013; De Bruyne *et al.*, 2012; Levin *et al.*, 2011). In this work, when using both models, the treatment group had significantly lower tumor mean K_T^{trans} and K_S^{trans}, suggesting the effective treatment effect of bevacizumab. In addition, the K^{trans} kurtosis of both the treatment and the control group increased along with the experiment, which indicated that K^{trans} distribution

evolved towards leptokurtosis. This observation is not consistent with a previous study in which the increase of kurtosis was correlated with the tumor chemotherapy response (Chang *et al.*, 2004). The skewness statistics in this work were all positive, and this means that the observed K^{trans} distributions' peaks were with low intensity region with a longer tail at the high intensity region. Consistent with the decreasing K^{trans} statistics in Figure 5(a), the increase of skewness reflects the shift of K^{trans} peak value towards the lower intensities. Few studies regarding the longitudinal change of K^{trans} histogram descriptors after therapy have been reported. This renders the use of kurtosis and skewness preliminary and challenging in DCE-MRI therapeutic response assessment.

The value of the additional PK parameter τ_i from the transcytolemmal water exchange analysis for therapeutic response assessment was demonstrated. Previously, τ_i has been shown to be potentially valuable for diagnostic assistance (Li *et al.*, 2005). In terms of treatment assessment, however, some studies concluded that τ_i may not be able to offer extra information for monitoring treatment response (Yankeelov *et al.*, 2007). In this work, the tumor mean τ_i of the treatment group increased in the experiment and was significantly higher than the corresponding values of the control group. As is presented in the theory (Landis *et al.*, 1999), $\tau_i = V/(P \cdot A)$ where P is the diffusional permeability of the cell membrane, A is the cell surface area and V is the volume of the cell. As a result, the increased τ_i of the treatment group could be a result of the increased cell size and/or decreased diffusional cell permeability. The diffusional cell membrane permeability may be reflected by the apparent diffusion coefficient (ADC) from diffusion-weighted imaging (DW-MRI). Future work with the inclusion of DW-MRI technique may improve the understanding of τ_i in therapeutic response assessment.

The introduction of biological subvolume (BV) based on τ_i distribution has been proved valuable for DCE-MRI therapeutic response assessment. Previous work has predicted that FXL holds when $\tau_i^{-1}/p_0 \gg |R_{1o0} - R_{1i}|$, where p_0 is the fractions of water molecules in EES, R_{1o0} is the native longitudinal relaxation rate of EES water molecules, and R_{1i} is the longitudinal relaxation rate of intracellular water molecules (Landis *et al.*, 1999). For the Day0 scan presented in Figure 2, the τ_i in BV ranged from about 10ms to 1s. If R_{1o0} was approximated by R_{10} and R_{1i} could be roughly estimated as R_1, then the observed mean $|R_1 - R_{10}|$ at the maximum enhancement time point was about $0.233 s^{-1}$, and its maximum value was around $0.952\ s^{-1}$. Given the range of p_0 as [0.13, 0.95] (Donahue *et al.*, 1995), it is possible that FXL could be invalid in some BV voxels with higher τ_i values. Without further knowledge of p_0, it is infeasible to do further quantitative evaluation of FXL condition distribution in BV. The BV volume ratio of both treatment/control groups decreased during the experiment. Although the treatment group was inclined to have higher BV volume ratio, no significant difference was observed. Future studies with histology report may validate the potential physiological meaning of BV.

The $K^{trans}_{S,BV}$ analysis within the BV was proved to be superior to the analysis in whole tumor. In Figure 7(a), the treatment group had a significantly lower mean $K^{trans}_{S,BV}$ value as early as after the first treatment delivery at Day2, while in Figure 5(a), the mean K^{trans}_{S} and K^{trans}_{T} across the tumor did not show significant differences between treatment/control groups until

Day9. When using mean $K^{trans}_{S,BV}$ and its CV as the biomarkers for treatment/control separation, the achieved accuracy was 68.8%, which was higher than the accuracy 62.5% using tumor mean K^{trans}_{S} and its CV and 50.0% using tumor mean K^{trans}_{T} and its CV, respectively. Furthermore, the spatial heterogeneity indices d_1 and d_2 of $K^{trans}_{S,BV}$ demonstrated significant difference between treatment/control groups at Day9. These results suggest that the SS model should be adopted in small animal DCE-MRI experiment for monitoring the early bevacizumab therapeutic response.

One of the contributions of our work is the longitudinal study of d_1 and d_2 change using *in vivo* small animal data. Although the theory of fractal dimensions were developed primarily for abstract mathematical objects, it can be applied to the real objects that may not come from fractal process. Biologically, the branching nature of the tumor vascularity is likely to be a fractal process, but it cannot be directly observed on current diagnostic MR images with the current imaging resolution (~1mm). In this work, the improved spatial resolution (156μm) makes the fractal dimension analysis appealing. As the tumor evolves, the periphery and the core of the tumor may have different enhancing rates during the CA uptake with a heterogeneous K^{trans} distribution (Su *et al.*, 2003). The inclusion of spatial heterogeneity information could provide supplementary information for capturing treatment response. As quantitative metrics describing the object complexity, high d_1 and d_2 values were associated with high degree of heterogeneity. Previous studies reported increased K^{trans} d_1 and d_2 values after the simulated treatment using digital tumor phantom (Rose *et al.*, 2009). In this work, however, both treatment/control groups had a decreasing trend of K^{trans} d_1 and d_2 when evaluating the whole tumor and the BV, and the treatment group had significantly higher $K^{trans}_{S,BV}$ d_1 and d_2 values at Day9. This inconsistency could be explained by the incomplete tumor regression. Nevertheless, the therapeutic response evaluation using d_1 and d_2 is far from straightforward and needs to be exploited with future studies with larger small animal population.

5. Conclusion

This study compares the use of SS model with transcytolemmal water exchange analysis versus the classic Tofts model for longitudinal therapeutic response assessment in a small animal anti-angiogenesis drug experiment. Results show that when using the K^{trans} information across the tumor, the performances of the two models in treatment/control differentiation were comparable. When the biological subvolume from the SS model was adopted, the PK parameters' metrics were capable of capturing the therapeutic effects as early as after the first treatment delivery, while the Tofts model analysis can only demonstrate the therapeutic effects after three treatment deliveries. Our results suggest a great potential of the SS model for DCE-MRI early therapeutic response assessment.

Supplementary Material

Refer to Web version on PubMed Central for supplementary material.

Acknowledgments

The small animal experiment was performed at the Duke Center for In Vivo Microscopy, an NIH/NIBIB National Biomedical Technology Resource Center (P41 EB015897). The authors wish to thank Dr. Herbert Hurwitz for assistance with obtaining Avastin and helpful discussions on how it might best be administered.

References

Abramson RG, Li X, Hoyt TL, Su P-F, Arlinghaus LR, Wilson KJ, Abramson VG, Chakravarthy AB, Yankeelov TE. Early assessment of breast cancer response to neoadjuvant chemotherapy by semi-quantitative analysis of high-temporal resolution DCE-MRI: preliminary results. Magn Reson Imaging. 2013; 31:1457–64. [PubMed: 23954320]

Aerts HJ, Velazquez ER, Leijenaar RT, Parmar C, Grossmann P, Carvalho S, Bussink J, Monshouwer R, Haibe-Kains B, Rietveld D. Decoding tumour phenotype by noninvasive imaging using a quantitative radiomics approach. Nature communications. 2014; 5

Ahearn T, Staff R, Redpath T, Semple S. The use of the Levenberg–Marquardt curve-fitting algorithm in pharmacokinetic modelling of DCE-MRI data. Phys Med Biol. 2005; 50:N85. [PubMed: 15843726]

Alic L, van Vliet M, van Dijke CF, Eggermont AMM, Veenland JF, Niessen WJ. Heterogeneity in DCE-MRI parametric maps: a biomarker for treatment response? Phys Med Biol. 2011; 56:1601–16. [PubMed: 21335648]

Allen M, Brown GJ, Miles NJ. Measurement of boundary fractal dimensions: review of current techniques. Powder Technology. 1995; 84:1–14.

Bartholdi, L.; Grigorchuk, R.; Nekrashevych, V. From fractal groups to fractal sets. Springer; 2003.

Cabrera AR, Cuneo KC, Desjardins A, Sampson JH, McSherry F, Herndon JE, Peters KB, Allen K, Hoang JK, Chang Z. Concurrent stereotactic radiosurgery and bevacizumab in recurrent malignant gliomas: a prospective trial. International Journal of Radiation Oncology* Biology* Physics. 2013; 86:873–9.

Chang YC, Huang CS, Liu YJ, Chen JH, Lu YS, Tseng WY. Angiogenic response of locally advanced breast cancer to neoadjuvant chemotherapy evaluated with parametric histogram from dynamic contrast-enhanced MRI. Phys Med Biol. 2004; 49:3593–602. [PubMed: 15446790]

Chang Z, Wang C. Treatment assessment of radiotherapy using MR functional quantitative imaging. World J Radiol. 2015; 7:1–6. [PubMed: 25628799]

Chen W, Giger ML, Li H, Bick U, Newstead GM. Volumetric texture analysis of breast lesions on contrast-enhanced magnetic resonance images. Magnetic Resonance in Medicine. 2007; 58:562–71. [PubMed: 17763361]

Choyke PL, Dwyer AJ, Knopp MV. Functional tumor imaging with dynamic contrast-enhanced magnetic resonance imaging. Journal of Magnetic Resonance Imaging. 2003; 17:509–20. [PubMed: 12720260]

Cohen MH, Gootenberg J, Keegan P, Pazdur R. FDA drug approval summary: bevacizumab (Avastin®) plus carboplatin and paclitaxel as first-line treatment of advanced/metastatic recurrent nonsquamous non-small cell lung cancer. The Oncologist. 2007; 12:713–8. [PubMed: 17602060]

Collins, D.; Walker, S.; Dzik-Jurasz, A.; Leach, M. Fractal analysis of parametric images derived from dynamic contrast enhanced MRI data in-vivo: methods for describing dispersion in parametric data. Proceedings of the International Society of Magnetic Resonance in Medicine; Toronto. 2003. p. 1269

DCE-MRI-Technical-Committee. DCE MRI Quantification Profile, Quantitative Imaging Biomarker Alliance. Radiological Society of North America; 2012.

De Bruyne S, Van Damme N, Smeets P, Ferdinande L, Ceelen W, Mertens J, Van De Wiele C, Troisi R, Libbrecht L, Laurent S. Value of DCE-MRI and FDG-PET/CT in the prediction of response to preoperative chemotherapy with bevacizumab for colorectal liver metastases. Brit J Cancer. 2012; 106:1926–33. [PubMed: 22596235]

Delongchamps NB, Beuvon F, Eiss D, Flam T, Muradyan N, Zerbib M, Peyromaure M, Cornud F. Multiparametric MRI is helpful to predict tumor focality, stage, and size in patients diagnosed with unilateral low-risk prostate cancer. Prostate Cancer P D. 2011; 14:232–7.

Donahue KM, Weisskoff RM, Parmelee DJ, Callahan RJ, Wilkinson RA, Mandeville JB, Rosen BR. Dynamic Gd-DTPA enhanced MRI measurement of tissue cell volume fraction. Magnetic resonance in medicine. 1995; 34:423–32. [PubMed: 7500882]

Fram EK, Herfkens RJ, Johnson GA, Glover GH, Karis JP, Shimakawa A, Perkins TG, Pelc NJ. Rapid calculation of T1 using variable flip angle gradient refocused imaging. Magn Reson Imaging. 1987; 5:201–8. [PubMed: 3626789]

Goh V, Ganeshan B, Nathan P, Juttla JK, Vinayan A, Miles KA. Assessment of response to tyrosine kinase inhibitors in metastatic renal cell cancer: CT texture as a predictive biomarker. Radiology. 2011; 261:165–71. [PubMed: 21813743]

Huang W, Li X, Chen Y, Li X, Chang M-C, Oborski MJ, Malyarenko DI, Muzi M, Jajamovich GH, Fedorov A. Variations of dynamic contrast-enhanced magnetic resonance imaging in evaluation of breast cancer therapy response: a multicenter data analysis challenge. Translational oncology. 2014; 7:153–66. [PubMed: 24772219]

Huang W, Li X, Morris EA, Tudorica LA, Seshan VE, Rooney WD, Tagge I, Wang Y, Xu J, Springer CS. The magnetic resonance shutter speed discriminates vascular properties of malignant and benign breast tumors in vivo. Proceedings of the National Academy of Sciences. 2008; 105:17943–8.

Hylton N. Dynamic contrast-enhanced magnetic resonance imaging as an imaging biomarker. J Clin Oncol. 2006; 24:3293–8. [PubMed: 16829653]

Jaffe CC. Measures of response: RECIST, WHO, and new alternatives. Journal of clinical oncology : official journal of the American Society of Clinical Oncology. 2006; 24:3245–51. [PubMed: 16829648]

Jain RK, Duda DG, Clark JW, Loeffler JS. Lessons from phase III clinical trials on anti-VEGF therapy for cancer. Nature clinical practice Oncology. 2006; 3:24–40.

Jiang Y, Nishikawa RM, Schmidt RA, Metz CE, Giger ML, Doi K. Improving breast cancer diagnosis with computer-aided diagnosis. Academic radiology. 1999; 6:22–33. [PubMed: 9891149]

Kershaw LE, Buckley DL. Precision in measurements of perfusion and microvascular permeability with T1-weighted dynamic contrast-enhanced MRI. Magnetic resonance in medicine. 2006; 56:986–92. [PubMed: 16986107]

Kety S. Blood–tissue exchange methods. Theory of blood-tissue exchange and its application to measurement of blood flow. Methods in medical research. 1960; 8:223–7.

Kim S, Loevner L, Quon H, Kilger A, Sherman E, Weinstein G, Chalian A, Poptani H. Prediction of response to chemoradiation therapy in squamous cell carcinomas of the head and neck using dynamic contrast-enhanced MR imaging. American Journal of Neuroradiology. 2010; 31:262–8. [PubMed: 19797785]

Kim S, Quon H, Loevner LA, Rosen MA, Dougherty L, Kilger AM, Glickson JD, Poptani H. Transcytolemmal water exchange in pharmacokinetic analysis of dynamic contrast - enhanced MRI data in squamous cell carcinoma of the head and neck. Journal of Magnetic Resonance Imaging. 2007; 26:1607–17. [PubMed: 17968962]

Kleppestø M, Larsson C, Groote I, Salo R, Vardal J, Courivaud F, Bjørnerud A. T2*-correction in dynamic contrast-enhanced MRI from double-echo acquisitions. Journal of Magnetic Resonance Imaging. 2014; 39:1314–9. [PubMed: 24123598]

Labadie C, Lee J-H, Vetek G, Springer C. Relaxographic imaging. Journal of Magnetic Resonance, Series B. 1994; 105:99–112. [PubMed: 7952937]

Lambin P, Rios-Velazquez E, Leijenaar R, Carvalho S, van Stiphout RGPM, Granton P, Zegers CML, Gillies R, Boellard R, Dekker A, Aerts HJWL. Consortium Q-C. Radiomics: Extracting more information from medical images using advanced feature analysis. Eur J Cancer. 2012; 48:441–6. [PubMed: 22257792]

Landis CS, Li X, Telang FW, Coderre JA, Micca PL, Rooney WD, Latour LL, Vétek G, Pályka I, Springer CS. Determination of the MRI contrast agent concentration time course in vivo following

bolus injection: effect of equilibrium transcytolemmal water exchange. Magnetic resonance in medicine. 2000; 44:563–74. [PubMed: 11025512]

Landis CS, Li X, Telang FW, Molina PE, Palyka I, Vetek G, Springer CS. Equilibrium transcytolemmal water-exchange kinetics in skeletal muscle in vivo. Magnetic Resonance in Medicine. 1999; 42:467–78. [PubMed: 10467291]

Levin VA, Bidaut L, Hou P, Kumar AJ, Wefel JS, Bekele BN, Prabhu S, Loghin M, Gilbert MR, Jackson EF. Randomized double-blind placebo-controlled trial of bevacizumab therapy for radiation necrosis of the central nervous system. International Journal of Radiation Oncology* Biology* Physics. 2011; 79:1487–95.

Li X, Priest RA, Woodward WJ, Tagge IJ, Siddiqui F, Huang W, Rooney WD, Beer TM, Garzotto MG, Springer CS Jr . Feasibility of shutter-speed DCE-MRI for improved prostate cancer detection. Magnetic resonance in medicine : official journal of the Society of Magnetic Resonance in Medicine / Society of Magnetic Resonance in Medicine. 2013; 69:171–8.

Li X, Rooney WD, Springer CS Jr . A unified magnetic resonance imaging pharmacokinetic theory: intravascular and extracellular contrast reagents. Magnetic resonance in medicine : official journal of the Society of Magnetic Resonance in Medicine / Society of Magnetic Resonance in Medicine. 2005; 54:1351–9.

Loveless ME, Halliday J, Liess C, Xu L, Dortch RD, Whisenant J, Waterton JC, Gore JC, Yankeelov TE. A quantitative comparison of the influence of individual versus population-derived vascular input functions on dynamic contrast enhanced-MRI in small animals. Magnetic Resonance in Medicine. 2012; 67:226–36. [PubMed: 21688316]

Murase K. Efficient method for calculating kinetic parameters using T1-weighted dynamic contrast-enhanced magnetic resonance imaging. Magnetic resonance in medicine. 2004; 51:858–62. [PubMed: 15065262]

Noebauer-Huhmann IM, Szomolanyi P, Juras V, Kraff O, Ladd ME, Trattnig S. Gadolinium-based magnetic resonance contrast agents at 7 Tesla: in vitro T1 relaxivities in human blood plasma. Investigative radiology. 2010; 45:554–8. [PubMed: 20697225]

O'Connor JP, Jackson A, Parker GJ, Jayson GC. DCE-MRI biomarkers in the clinical evaluation of antiangiogenic and vascular disrupting agents. Brit J Cancer. 2007; 96:189–95. [PubMed: 17211479]

O'Connor JP, Jackson A, Parker GJ, Roberts C, Jayson GC. Dynamic contrast-enhanced MRI in clinical trials of antivascular therapies. Nature reviews Clinical oncology. 2012; 9:167–77.

O'Connor JP, Rose CJ, Jackson A, Watson Y, Cheung S, Maders F, Whitcher BJ, Roberts C, Buonaccorsi GA, Thompson G, Clamp AR, Jayson GC, Parker GJ. DCE-MRI biomarkers of tumour heterogeneity predict CRC liver metastasis shrinkage following bevacizumab and FOLFOX-6. British journal of cancer. 2011; 105:139–45. [PubMed: 21673686]

Padhani AR, Leach MO. Antivascular cancer treatments: functional assessments by dynamic contrast-enhanced magnetic resonance imaging. Abdominal imaging. 2005; 30:324–41. [PubMed: 15688112]

Parker GJ, Suckling J, Tanner SF, Padhani AR, Revell PB, Husband JE, Leach MO. Probing tumor microvascularity by measurement, analysis and display of contrast agent uptake kinetics. Journal of Magnetic Resonance Imaging. 1997; 7:564–74. [PubMed: 9170043]

Rose CJ, Mills SJ, O'Connor JP, Buonaccorsi GA, Roberts C, Watson Y, Cheung S, Zhao S, Whitcher B, Jackson A, Parker GJ. Quantifying spatial heterogeneity in dynamic contrast-enhanced MRI parameter maps. Magnetic resonance in medicine : official journal of the Society of Magnetic Resonance in Medicine / Society of Magnetic Resonance in Medicine. 2009; 62:488–99.

Schabel MC, Parker DL. Uncertainty and bias in contrast concentration measurements using spoiled gradient echo pulse sequences. Phys Med Biol. 2008; 53:2345. [PubMed: 18421121]

Schwarz G. Estimating the dimension of a model. The annals of statistics. 1978; 6:461–4.

Sokal, RR.; Rohlf, FJ. The principles and practice of statistics in biological research. WH Freeman; San Francisco: 1981. Biometry.

Su M-Y, Cheung Y-C, Fruehauf JP, Yu H, Nalcioglu O, Mechetner E, Kyshtoobayeva A, Chen S-C, Hsueh S, McLaren CE, Wan Y-L. Correlation of dynamic contrast enhancement MRI parameters

with microvessel density and VEGF for assessment of angiogenesis in breast cancer. Journal of Magnetic Resonance Imaging. 2003; 18:467–77. [PubMed: 14508784]

Subashi E, Choudhury KR, Johnson GA. An analysis of the uncertainty and bias in DCE-MRI measurements using the spoiled gradient-recalled echo pulse sequence. Medical physics. 2014; 41:032301. [PubMed: 24593738]

Subashi E, Moding EJ, Cofer GP, MacFall JR, Kirsch DG, Qi Y, Johnson GA. A comparison of radial keyhole strategies for high spatial and temporal resolution 4D contrast-enhanced MRI in small animal tumor models. Medical physics. 2013; 40:022304. [PubMed: 23387766]

Tofts PS, Kermode AG. Measurement of the blood? brain barrier permeability and leakage space using dynamic MR imaging. 1. Fundamental concepts. Magnetic Resonance in Medicine. 1991; 17:357–67. [PubMed: 2062210]

van der Heide UA, Houweling AC, Groenendaal G, Beets-Tan RG, Lambin P. Functional MRI for radiotherapy dose painting. Magn Reson Imaging. 2012; 30:1216–23. [PubMed: 22770686]

Wang C, Horton JK, Yin F-F, Chang Z. Assessment of Treatment Response With Diffusion-Weighted MRI and Dynamic Contrast-Enhanced MRI in Patients With Early-Stage Breast Cancer Treated With Single-Dose Preoperative Radiotherapy Initial Results. Technology in cancer research & treatment. 2015 1533034615593191.

Wang C, Subashi E, Yin F-F, Chang Z. Dynamic fractal signature dissimilarity analysis for therapeutic response assessment using dynamic contrast-enhanced MRI. Medical physics. 2016; 43:1335–47. [PubMed: 26936718]

Yang X, Knopp MV. Quantifying tumor vascular heterogeneity with dynamic contrast-enhanced magnetic resonance imaging: a review. Journal of biomedicine & biotechnology. 2011; 2011:732848. [PubMed: 21541193]

Yankeelov TE, Lepage M, Chakravarthy A, Broome EE, Niermann KJ, Kelley MC, Meszoely I, Mayer IA, Herman CR, McManus K. Integration of quantitative DCE-MRI and ADC mapping to monitor treatment response in human breast cancer: initial results. Magn Reson Imaging. 2007; 25:1–13. [PubMed: 17222711]

Yankeelov TE, Rooney WD, Huang W, Dyke JP, Li X, Tudorica A, Lee JH, Koutcher JA, Springer CS Jr . Evidence for shutter-speed variation in CR bolus-tracking studies of human pathology. NMR Biomed. 2005; 18:173–85. [PubMed: 15578708]

Yankeelov TE, Rooney WD, Li X, Springer CS. Variation of the relaxographic “shutter-speed” for transcytolemmal water exchange affects the CR bolus-tracking curve shape. Magnetic resonance in medicine. 2003; 50:1151–69. [PubMed: 14648563]

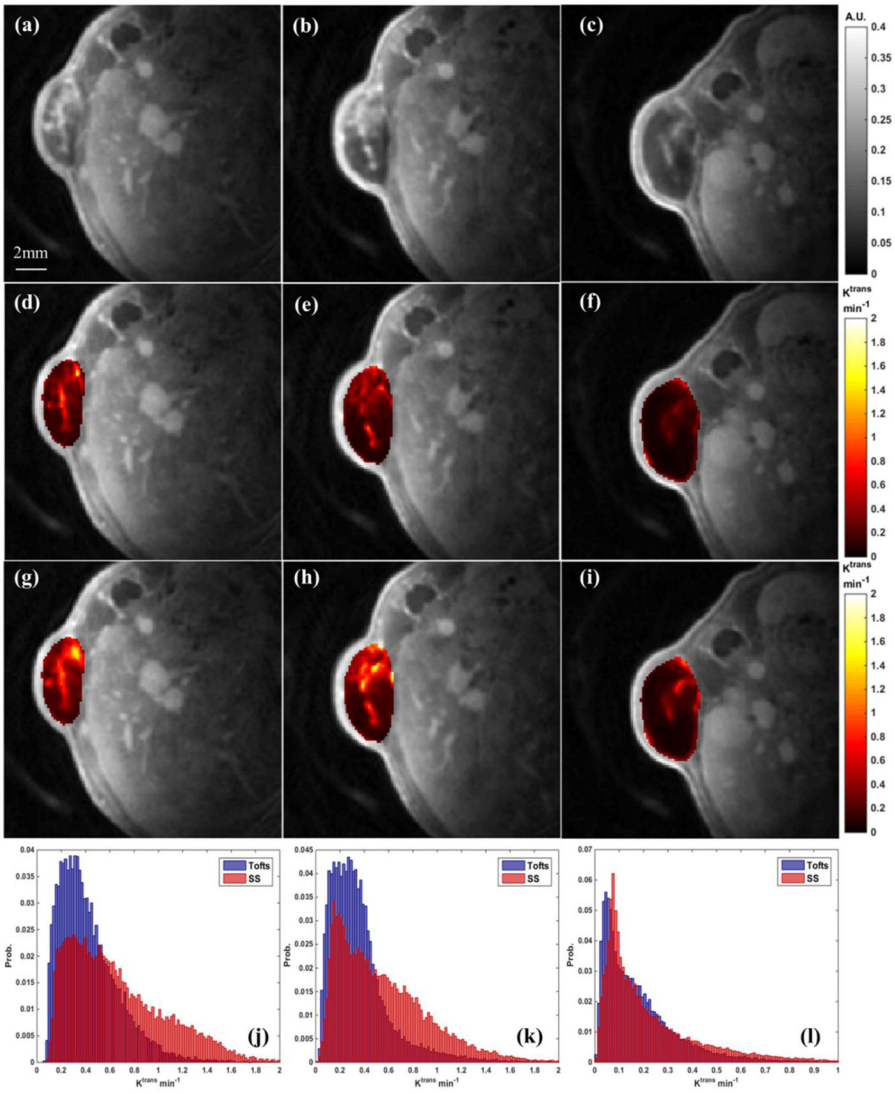

Figure 1.

A demonstration of K^{trans} from a selected animal at three scan days. Left column: Day0; middle column: Day2; right column: Day9. First row: post-injection T1w DCE image; 2nd row: K_T^{trans} maps from the Tofts model; 3rd row: K_S^{trans} maps from the SS model; 4th row: joint histogram of K_T^{trans} and K_S^{trans}. The tumor mean values of this animal are: Day0: K_T^{trans}=0.429min^{-1}, K_S^{trans}=0.661min^{-1}; Day2: K_T^{trans}=0.361min^{-1}, K_S^{trans}=0.559min^{-1}; Day9: K_T^{trans}=0.153min^{-1}, K_S^{trans}=0.229min^{-1}

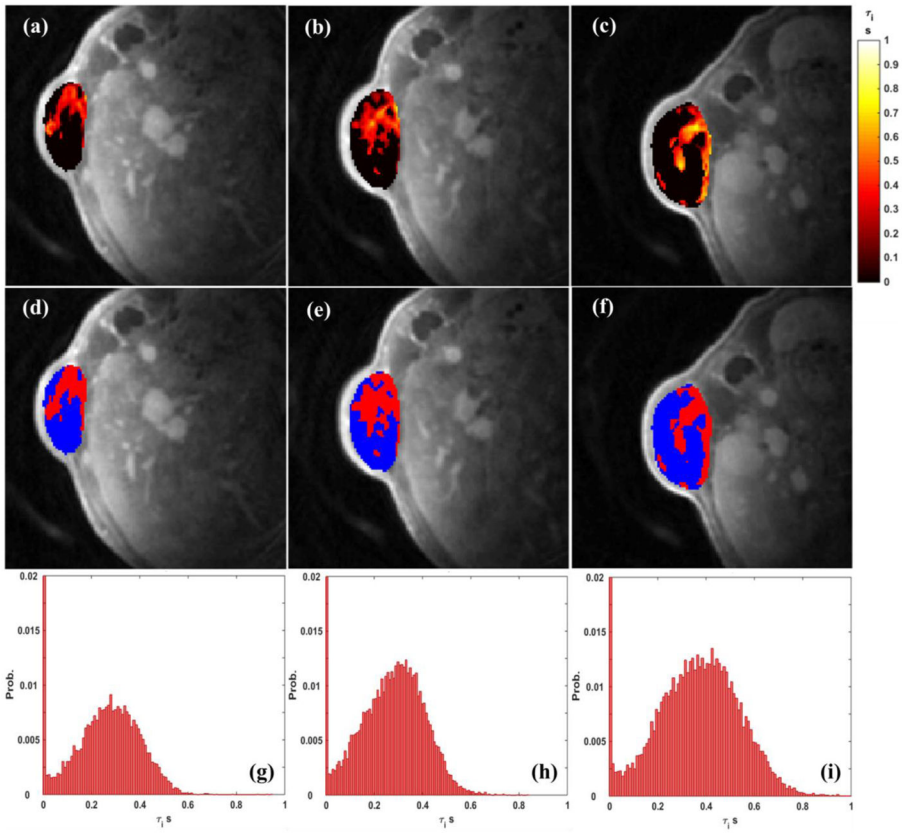

Figure 2.

A demonstration of τ_i from a selected animal at three scan days. Left column: Day0; middle column: Day2; right column: Day9. First row: the τ_i maps across the tumor; 2nd row: the identified BV (red area) within the tumor; 3rd row: the τ_i histograms. The tumor mean values of this animal are: Day0: τ_i = 0.159 s; Day2: τ_i = 0.170 s; Day9: τ_i = 0.193 s

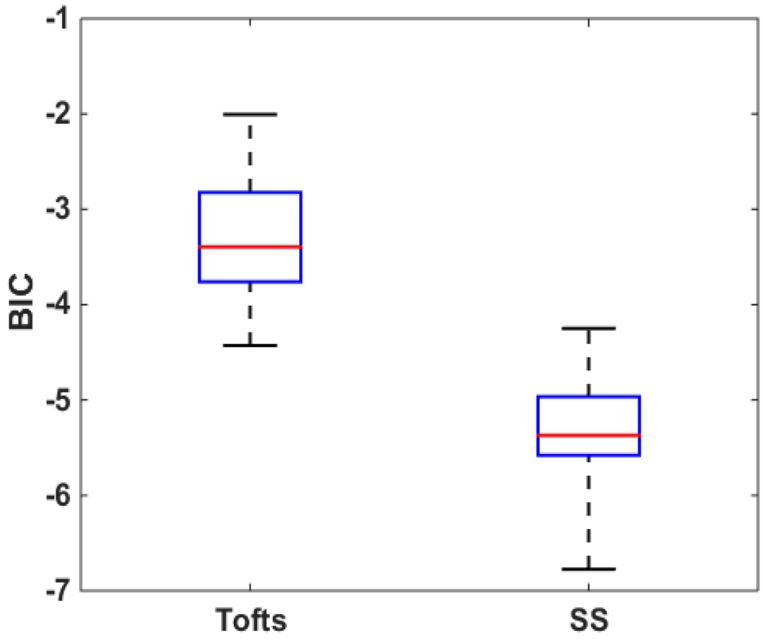

Figure 3.

The BIC statistics of the Tofts model and the SS models of all analyzed scans. The red horizontal line indicates the median value and the whiskers indicate ± 1.5 interquartile range (IQR)

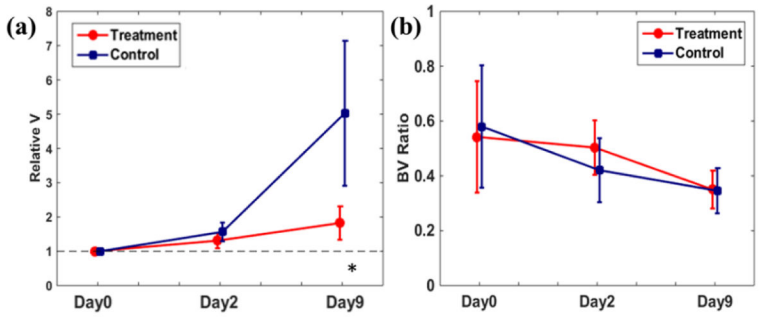

Figure 4.

Comparisons of tumor growth rate (a) and the ratio of identified BV to tumor volume (b). The error bar represents the group standard deviation. * indicates statistical significance

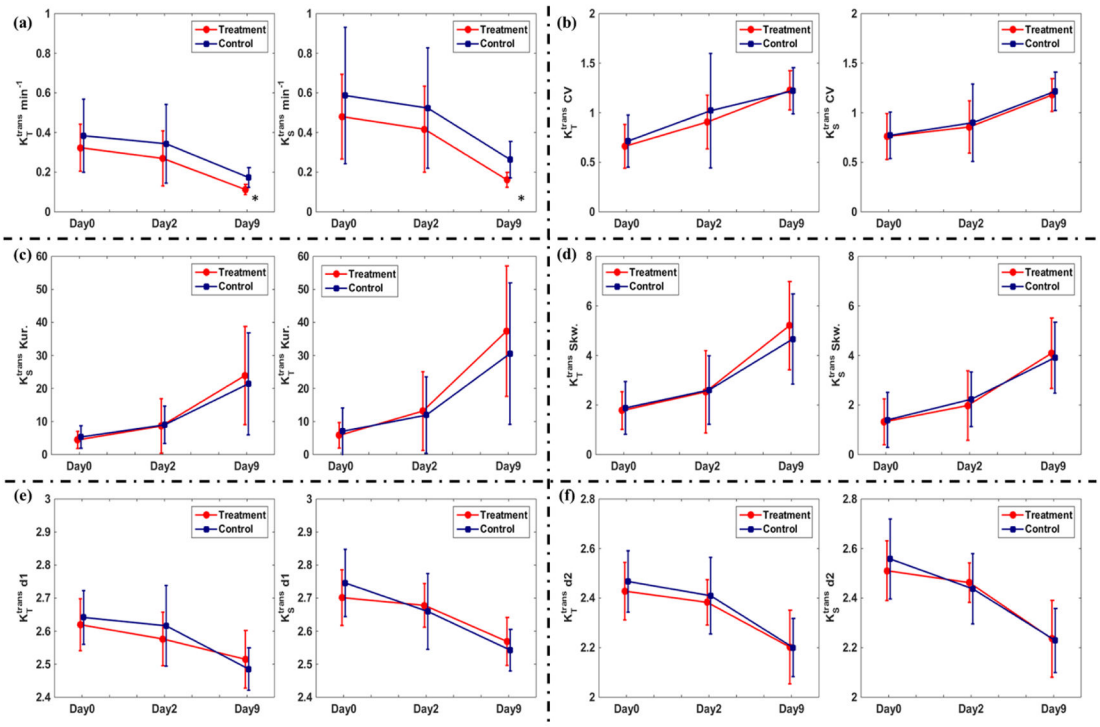

Figure 5.

Comparisons of K_T^{trans} and K_S^{trans} at three treatment days in terms of tumor mean value (a), CV (b), kurtosis (b), skewness (b), d_1 (e) and d_2 (f) at three treatment days. The error bar represents the group standard deviation. At Day9, the treatment group had significantly lower (indicated by *) K_T^{trans} and K_S^{trans}.

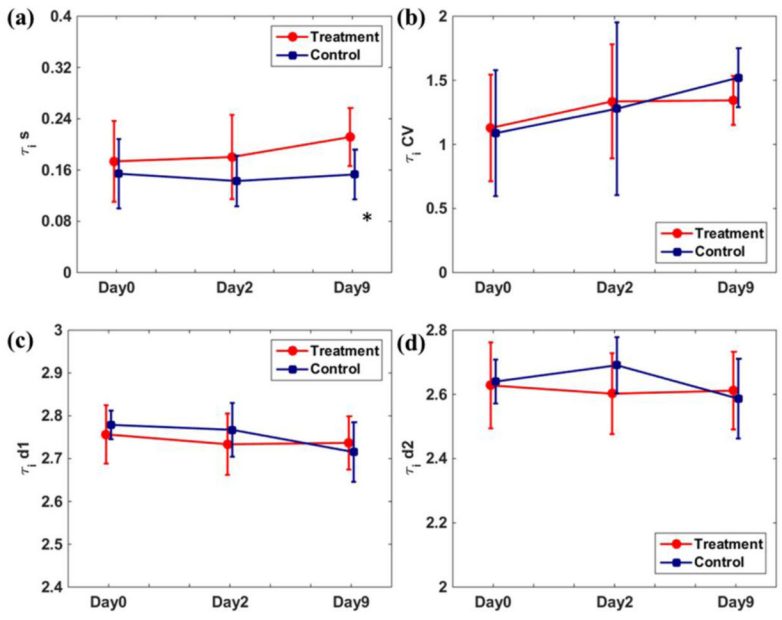

Figure 6.

Comparisons of τ_i mean value (a), CV (b), d_1 (c) and d_2 (d) at three treatment days. The error bar represents the group standard deviation. At Day9, the treatment group had significantly higher (indicated by *) τ_i.

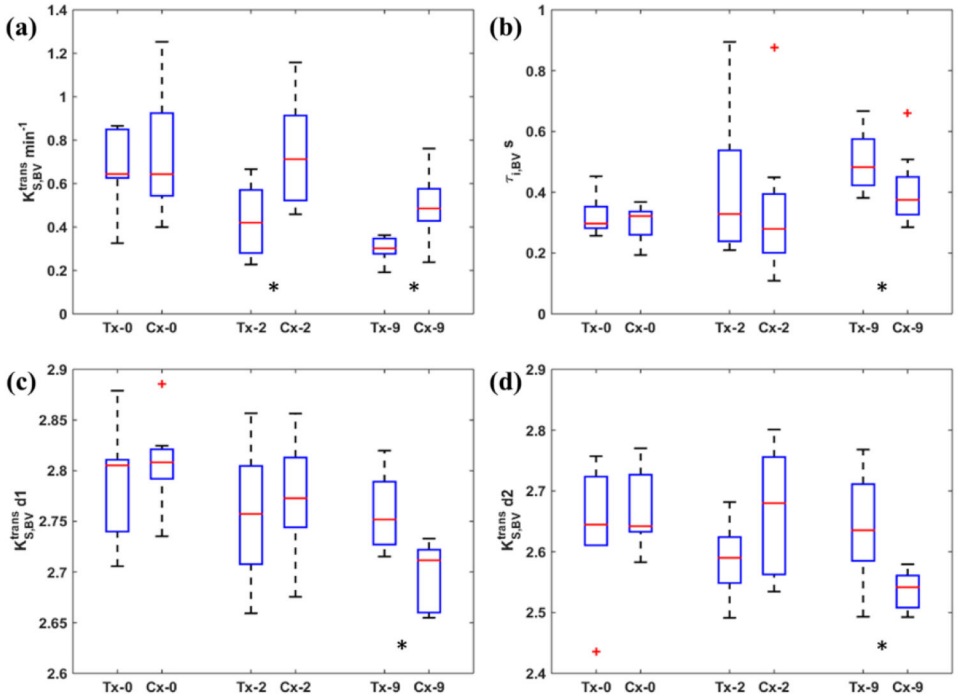

Figure 7.

Comparisons of mean $K^{trans}_{S,BV}$ (a), mean $\tau_{i,BV}$ (b), $K^{trans}_{S,BV}$ d_1 (c) and d_2 (d) at three treatment days. Tx = treatment group; Cx = control group. The red horizontal line indicates the median value and the whiskers indicate ± 1.5 interquartile range (IQR). At Day2, the treatment group had significantly lower (indicated by *) $K^{trans}_{S,BV}$; At Day9 the treatment group had significantly lower (indicated by *) $K^{trans}_{S,BV}$, $\tau_{i,BV}$ and $K^{trans}_{S,BV}$ d_1 and d_2 values

Table 1

The results of treatment/control group classification using SVM

		SVM Input	Classification Accuracy	
			Day2	Day9
Tofts Model	*Whole tumor*	Mean K_T^{trans}	43.8%	68.8%
		(Mean K_T^{trans}, CV)	50.0%	87.5%
		(Mean K_T^{trans}, Kurtosis, Skewness)	31.3%	56.3%
		(Mean K_T^{trans}, d_1, d_2)	43.8%	75.0%
SS Model	*Whole tumor*	Mean K_S^{trans}	50.0%	68.8%
		(Mean K_S^{trans}, CV)	62.5%	87.5%
		(Mean K_S^{trans}, Kurtosis, Skewness)	43.8%	62.5%
		(Mean K_S^{trans}, d_1, d_2)	50.0%	56.3%
		Mean τ_i	56.3%	56.3%
		(Mean τ_i, CV)	37.5%	68.8%
		(Mean τ_i, d_1, d_2)	50.0%	56.3%
	BV	Mean $K_{S,BV}^{trans}$	50.0%	87.5%
		(Mean $K_{S,BV}^{trans}$, CV)	68.8%	87.5%
		(Mean $K_{S,BV}^{trans}$, Kurtosis, Skewness)	68.8%	75.0%
		(Mean $K_{S,BV}^{trans}$, d_1, d_2)	68.8%	75.0%
		Mean $\tau_{i,BV}$	43.8%	56.3%
		(Mean $\tau_{i,BV}$, CV)	43.8%	62.5%
		(Mean $\tau_{i,BV}$, Kurtosis, Skewness)	37.5%	56.3%
		(Mean $\tau_{i,BV}$, d_1, d_2)	56.3%	56.3%